

# HBVLA: Pushing 1-Bit Post-Training Quantization for Vision-Language-Action Models

Xin Yan<sup>1</sup>, Zhenglin Wan<sup>2</sup>, Feiyang Ye, Xingrui Yu<sup>3\*</sup>, Hangyu Du<sup>4</sup>, Yang You<sup>2</sup>, Ivor Tsang<sup>3</sup>

<sup>1</sup>School of Artificial Intelligence, Beijing Normal University, Beijing, China

<sup>2</sup>Department of Computer Science, National University of Singapore, Singapore

<sup>3</sup>Centre for Frontier AI Research, Agency for Science, Technology and Research (A\*STAR), Singapore

<sup>4</sup>College of Design and Engineering, National University of Singapore, Singapore

yu\_xingrui@a-star.edu.sg

## Abstract

Vision-Language-Action (VLA) models enable instruction-following embodied control, but their large compute and memory footprints hinder deployment on resource-constrained robots and edge platforms. While reducing weights to 1-bit precision through binarization can greatly improve efficiency, existing methods fail to narrow the distribution gap between binarized and full-precision weights, causing quantization errors to accumulate under long-horizon closed-loop execution and severely degrade actions. To fill this gap, we propose HBVLA, a VLA-tailored binarization framework. First, we use a policy-aware enhanced Hessian to identify weights that are truly critical for action generation. Then, we employ a sparse orthogonal transform for non-salient weights to induce a low-entropy intermediate state. Finally, we quantize both salient and non-salient weights in the Harr domain with group-wise 1-bit quantization. We have evaluated our approach on different VLAs: on LIBERO, quantized OpenVLA-OFT retains 92.2% of full-precision performance; on SimplerEnv, quantized CogAct retains 93.6%, significantly outperforming state-of-the-art binarization methods. We further validate our method on real-world evaluation suite and the results show that HBVLA incurs only marginal success-rate degradation compared to the full-precision model, demonstrating robust deployability under tight hardware constraints. Our work provides a practical foundation for ultra-low-bit quantization of VLAs, enabling more reliable deployment on hardware-limited robotic platforms.

## Introduction

In recent years, Vision-Language-Action (VLA) models have emerged as a powerful paradigm for instruction-following embodied control by integrating visual perception, language understanding, and action generation within a single policy. Representative VLAs, such as RT-2 (Zitkovich et al. 2023), OpenVLA (Kim et al. 2024), and CogACT (Li et al. 2024a), have demonstrated strong performance on a wide range of manipulation tasks, including long-horizon instruction execution and generalization across diverse objects and scenes. These advances are largely enabled by large-scale model parameters and extensive robot datasets, which

together provide high representation capacity and robust instruction grounding. However, these capabilities come with substantial computational demands and high memory usage, posing significant challenges for deployment on resource-constrained robotic platforms and edge devices where real-time, closed-loop control is required.

Post-Training Quantization (PTQ) (Nagel et al. 2019, 2020; Krishnamoorthi 2018) has gained significant traction due to its efficiency and practicality. Unlike quantization-aware training (QAT) (Jacob et al. 2018), which requires access to training data and retraining the network, PTQ operates on frozen parameters and uses a small calibration set to determine quantization parameters and rounding decisions. Recent PTQ methods have shown promising results in reducing weight and activation bitwidths for large models (Lin et al. 2024). Despite progress in 8-bit and 4-bit quantization for VLAs (Fang et al. 2025), the scale and deployment constraints of modern VLAs still call for more aggressive compression. Neural network binarization, which reduces weight precision to a single bit, is a promising direction toward ultra-low-bit quantization ( $\leq 2$  bits). However, directly transferring binary PTQ methods from large language models (LLMs) and vision-language models (VLMs) to VLAs is often ineffective. Unlike LLMs or VLMs that are optimized and evaluated on perplexity or feature fidelity, VLA policies output continuous actions that are executed in a closed-loop physical process. As a result, even subtle quantization-induced action deviations can be amplified by contact dynamics and compound over long-horizon execution, leading to catastrophic failures such as unstable grasps or large trajectory drift. This fundamental mismatch calls for ultra-low-bit quantization methods specifically tailored to preserving VLA policy behavior.

To minimize quantization error during the binarization process, we revisit the solutions for the binarization objective. Our analysis reveal that: (1) Different components of a VLA exhibit different sensitivity to quantization. We evaluate the sensitivity of different components in VLAs, including the vision encoder, projector, language model, and action model. As shown in Figure 4, the vision model exhibits considerable robustness to quantization than other components, barely affecting the performance; the language model exhibits less sensitivity to quantization; the projector

\*Corresponding author.

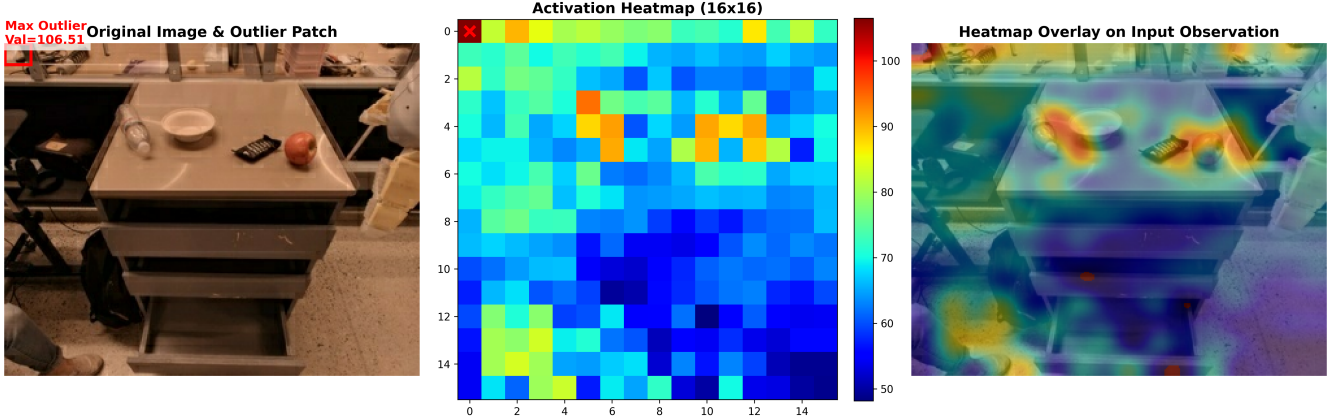


Figure 1: **Left:** The original observation highlighting a background artifact with an extreme activation magnitude (Val=106.5). **Middle:** The raw activation heatmap reveals an optimization landscape disproportionately dominated by these statistical outliers. **Right:** The overlay confirms the *misalignment*: the model’s physical sensitivity is hijacked by distractors (e.g., the water bottle and background clutter) rather than the task-critical target (the apple), visually evidencing the *dual dominance* problem.

and action model exhibit considerable sensitivity to quantization. (2) The current approach relies on Hessian (e.g.,  $\mathbf{H} = \mathbf{X}\mathbf{X}^\top$ ) to estimate weight importance. However, as visualized in Figure 1, we observe that VLA activation maps suffer from a dual dominance problem where they are statistically skewed by high-magnitude background outliers and further overwhelmed by the massive numerical visual token imbalance, directly leading to the inaccurate identification of salient weights that are critical for action. (3) Standard transforms like Haar fail here because VLA weights mix different modalities. Pairing different columns creates large value jumps which become outliers that introduce noise and ruin the accuracy of 1-bit quantization.

Based on these observations, we design **HBVLA**, an ultra-low-bit post-training binarization strategy tailored to VLAs. Our approach first partitions model weights based on a *policy-aware* saliency criterion, refining the Hessian with a token-level importance matrix to protect critical columns against action-sensitive degradation. For non-salient weights, we employ a *sparse orthogonal transform* to induce a low-entropy intermediate state. This maximizes Haar energy compaction, effectively suppressing high-pass heterogeneity to ensure stable binarization. Finally, both subsets are quantized in the Haar domain using frequency-aware grouping. Crucially, we apply shared-mean binarization specifically to the non-salient weights, balancing storage efficiency and quantization error minimization. Our key contributions can be summarized as follows:

- We evaluate the sensitivity of different components in VLAs. On average, the vision encoder exhibits considerable sensitivity to quantization.
- We propose HBVLA, a novel 1-bit post-training quantization framework. By combining policy-grounded saliency with spectral transformation, we effectively bridge the gap between aggressive 1-bit compression and precise embodied control.

- We push post-training quantization to bit-level for large VLAs in terms of three different benchmarks and three different models. From our experiments, our HBVLA outperforms SOTA binary PTQ methods adapted from LLMs and VLMs.

## Related Work

### Vision-Language-Action Models.

VLAs represent a major advancement in embodied AI, enabling end-to-end policies that directly map multimodal observations to robotic control. Typical VLA models, such as RT-2 (Zitkovich et al. 2023), OpenVLA (Kim et al. 2024), and UniVLA (Bu et al. 2025), extend pretrained VLMs (Karamcheti et al. 2024) by discretizing actions into tokens to generate executable sequences. Conversely, a second line of work prioritizes temporal fidelity and high-frequency control by modeling actions directly in the continuous domain. This is typically achieved with powerful generative decoders, such as the diffusion policies in Octo (Team et al. 2024) and CogACT (Li et al. 2024a), or the flow-matching network in  $\pi_0$  (Black et al. 2026), which excel at synthesizing smooth and precise dynamic trajectories. However, prohibitive memory demands hinder the deployment of these generative policies. Although quantization has been investigated in works like BitVLA (Wang et al. 2025a) and SQIP (Park et al. 2025), these approaches largely depend on QAT. While QAT can be effective, it incurs substantial computational overhead and necessitates access to large-scale robotic datasets, making it impractical for rapid adaptation. Consequently, the potential of low-bit PTQ remains conspicuously under-explored within embodied AI. This work aims to fill this critical gap, positing that quantization is not merely an incremental optimization but a foundational component required to unlock the practical deployment of generalist VLA models.

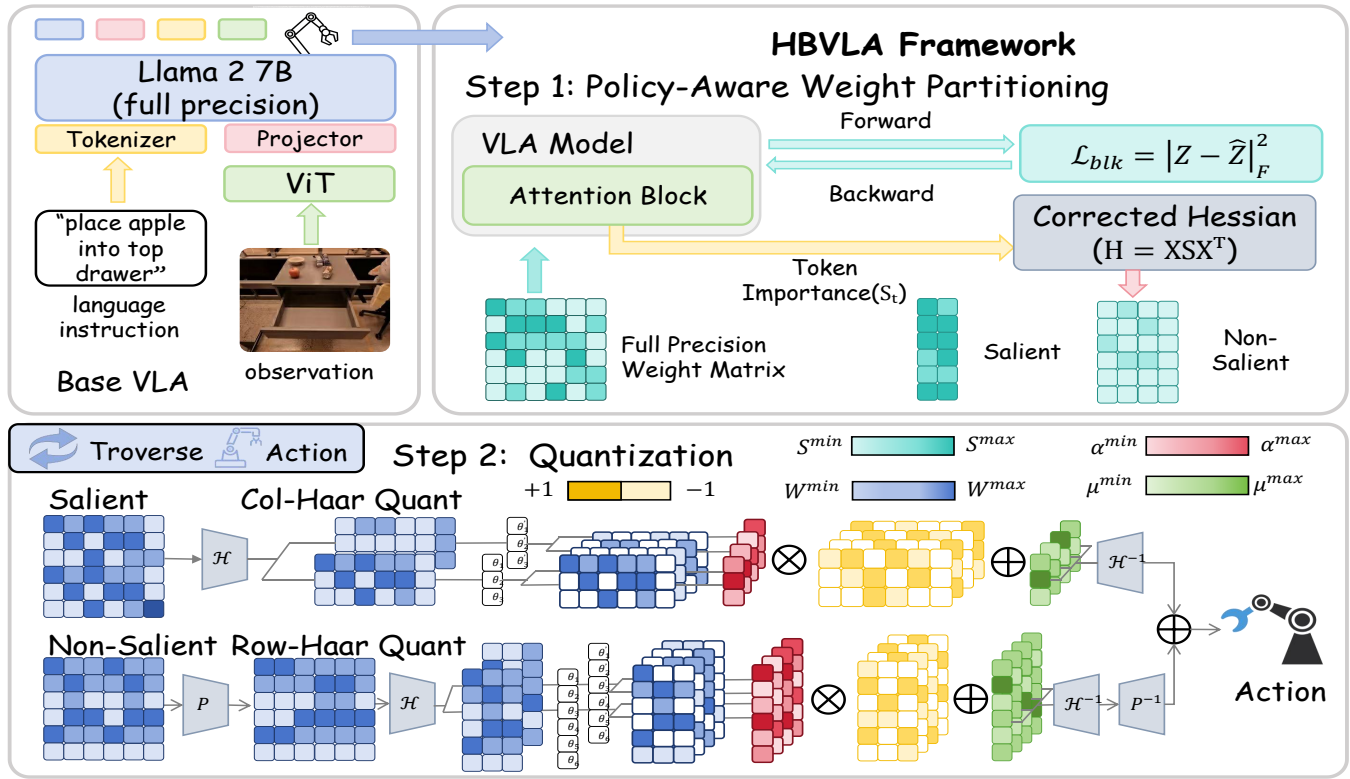


Figure 2: The pipeline of our **HBVLA** framework consists of two steps: (i) In Step 1, we establish a block-wise gradient probe to derive token importance scores ( $S_t$ ) and construct a **Corrected Hessian** proxy to identify *functionally salient* weights grounded in the policy. (ii) In Step 2, we apply a hybrid quantization strategy: salient weights undergo high-fidelity residual quantization, while non-salient weights are processed via sparse orthogonal transform ( $P$ ) and Haar wavelet transform ( $\mathcal{H}$ ) prior to group-wise 1-bit quantization.

## Network Binarization

Network binarization, a radical form of quantization that constrains both weights and activations to binary values (typically  $\pm 1$ ), has emerged as a pivotal technique for compressing neural networks while enabling efficient bitwise operations. Most existing binarization methods rely on QAT, where the training process explicitly accounts for quantization errors. To address the non-differentiability of the sign function, Straight-Through Estimators (STE) (Bengio, Leonard, and Courville 2013) are commonly employed to enable gradient propagation. BinaryConnect (Courbariaux, Bengio, and David 2015) and BWN pioneered weight binarization while retaining full-precision activations, whereas XNOR-Net (Rastegari et al. 2016) extended this paradigm by binarizing both weights and activations for maximal efficiency. The adaptation of binarization to transformers (Vaswani et al. 2017) faced unique challenges due to their reliance on attention modules. BiT (Liu et al. 2022b) pioneered transformer-specific strategies by incorporating elastic binarization with learnable scaling factors, and Eco-Former (Liu et al. 2022a) mapped the original queries and keys into low-dimensional binary codes in Hamming space via kernelized hashing. While LLM binarization has advanced through methods like PB-LLM (Yuan, Shang, and Dong 2024), BiLLM (Huang et al. 2024), and ARB-

LLM (Li et al. 2025), HBLLM (Chen, Ye, and Jiang 2025) introduced a structured framework based on Haar transforms to enhance expressive capacity by frequency decomposition. While Bi-VLM (Wang et al. 2025b) subsequently extended binarization to multimodal models via Gaussian quantile partitioning, it fails to capture critical activation columns. Building on the frequency-aware methodology of HBLLM, we propose a novel framework tailored for VLA models.

## Methodology

### Method Overview

We define the objective of HBVLA under the policy-preserving binary quantization setting. From a global perspective, we frame the quantization as an optimization problem to identify the optimal binary parameter configuration  $\hat{\theta}^*$  such that the induced policy  $f_{\hat{\theta}}$  minimizes the KL divergence to the full-precision policy  $f_{\theta}$ :

$$\hat{\theta}^* = \arg \min_{\hat{\theta}} \mathbb{E}_{x \sim \mathcal{D}} [D_{\text{KL}}(f_{\theta}(\cdot | x) \| f_{\hat{\theta}}(\cdot | x))]. \quad (1)$$

For the quantization of a matrix layer  $\mathbf{W}$ , the objective expressed in the Frobenius norm is formulated as:

$$\min_{\widehat{\mathbf{W}}} \left\| \mathbf{W} \mathbf{X} - \widehat{\mathbf{W}} \mathbf{X} \right\|_F^2, \quad (2)$$

where  $\mathbf{X}$  is the input of the matrix layer.

We emphasize that our approach does not aim to solve these objective functions via explicit end-to-end optimization. Instead, this formulation serves as a conceptual framework that guides our method design. The actual quantization process is based on a set of heuristics and structure-aware strategies that approximate these objectives in a computationally efficient manner. To this end, our method HBVLA adapts the efficient Haar transform into a unified pipeline tailored for VLAs. As shown in Figure 2, we begin by computing a policy-aware Hessian to identify salient weights critical for action. For the remaining non-salient weights, we apply a structured sparse orthogonal transform prior to the Haar transform. This aligns weight columns into a low-entropy state to suppress high-frequency noise. Subsequently, we perform **residual-aware refinement**, where salient columns are quantized via a column Haar transform to compensate for non-salient approximation errors.

### Policy-Aware Weight Partitioning

A critical challenge in quantizing VLAs is identifying salient weights, where quantization errors significantly degrade the continuous action policy. Saliency is typically assessed using either the magnitude or the Hessian-based metric. While Hessian-based methods generally offer higher precision, standard Hessian metrics defined as  $\mathbf{H} = \mathbf{XX}^\top = \sum_{t=1}^N \mathbf{x}_t \mathbf{x}_t^\top$  fail to capture policy-relevant signals in VLAs because they suffer from a **dual dominance** problem where the metric is dominated by redundant background or noisy outliers and overwhelmed numerically by the massive visual token imbalance. This distortion drowns out the sparse but instruction-conditioned signals essential for robotic control.

To address this issue, we propose a **policy-aware rectified Hessian** that reweights each token’s contribution according to its influence on action generation. This attenuates the impact of abundant visual tokens and outliers while emphasizing task-critical tokens. Specifically, we replace the uniform token aggregation in the standard Hessian with a token-weighted one:

$$\tilde{\mathbf{H}} \triangleq \mathbf{XSX}^\top = \sum_{t=1}^N s_t \mathbf{x}_t \mathbf{x}_t^\top, \quad (3)$$

where the related proof details are provided in Appendix .

In order to obtain the token-importance matrix  $\mathbf{S}$  efficiently, we adopt a block-wise gradient backpropagation method (Xue et al. 2025) along the action pathway. By limiting the backpropagation scope to the local block, we effectively capture the causal influence of each token on the policy’s intermediate features. Consequently, these gradient signals are utilized to formulate the rectified Hessian matrix for saliency estimation. This approach ensures that the binarization error budget is allocated based on functional criticality rather than raw magnitude, making the metric robust to modality imbalance and sporadic vision outliers. The pipeline proceeds as follows:

**Forward.** The block is defined as a residual attention module in the action pathway,  $\Phi(\mathbf{X}) \triangleq \mathbf{X} + \text{MHSA}(\mathbf{X})$ ,

together with its quantized counterpart  $\hat{\Phi}(\cdot)$  under the current binary weights. Given the same input  $\mathbf{X} \in \mathbb{R}^{d \times N}$ , the corresponding outputs are

$$\mathbf{Z} = \Phi(\mathbf{X}), \quad \hat{\mathbf{Z}} = \hat{\Phi}(\mathbf{X}), \quad (4)$$

and the binarization-induced deviation of this block is measured by

$$\mathcal{L}_{\text{blk}} = \|\mathbf{Z} - \hat{\mathbf{Z}}\|_F^2. \quad (5)$$

This block alignment loss provides a lightweight calibration objective that isolates the local distortion introduced by binarization, avoiding confounding factors from end-to-end policy optimization.

**Backward.** A single, locally isolated backpropagation on  $\mathcal{L}_{\text{blk}}$  captures gradients at the attention projections  $(Q, K, V, O)$ , identifying the primary pathways where binarization noise distorts the attention mechanism. Let  $\mathcal{P} = \{Q, K, V, O\}$  index the projection outputs  $\mathbf{Y}^{(p)} \in \mathbb{R}^{d_p \times N}$ . The cached gradients are

$$\mathbf{G}^{(p)} \triangleq \frac{\partial \mathcal{L}_{\text{blk}}}{\partial \mathbf{Y}^{(p)}} \in \mathbb{R}^{d_p \times N}, \quad p \in \mathcal{P}. \quad (6)$$

A larger  $\|\mathbf{G}_{:,t}^{(p)}\|$  indicates that perturbing token  $t$  at projection  $p$  would incur a larger deviation at the block output, hence stronger sensitivity to binarization along the action computation route.

**Process Grad.** Token-wise importance is computed *per projection* by column-wise  $\ell_2$  aggregation of the cached gradients, capturing how strongly each token affects the attention computation along a specific linear pathway:

$$a_t^{(p)} \triangleq \frac{1}{d_p} \|\mathbf{G}_{:,t}^{(p)}\|_2, \quad p \in \mathcal{P}. \quad (7)$$

Subsequently, we encapsulate these scores into a diagonal importance matrix for each projection:

$$\mathbf{S}_{\text{attn}}^{(p)} \triangleq \text{Diag}(a_1^{(p)}, \dots, a_N^{(p)}), \quad p \in \mathcal{P}. \quad (8)$$

Leveraging this weighting term, we derive the corresponding rectified Hessian proxy:

$$\tilde{\mathbf{H}}_{\text{attn}}^{(p)} \triangleq \mathbf{XS}_{\text{attn}}^{(p)} \mathbf{X}^\top, \quad p \in \mathcal{P}, \quad (9)$$

which is used for saliency estimation of the *specific* attention projection  $p \in \{Q, K, V, O\}$ . Since  $\mathbf{S}_{\text{attn}}^{(p)}$  is derived from gradient magnitudes, it effectively filters token importance by suppressing features exerting negligible influence on action generation, while prioritizing those critical for preserving instruction-grounded semantics. This projection-wise reweighting prevents  $\tilde{\mathbf{H}}_{\text{attn}}^{(p)}$  from being dominated by the massive visual token imbalance or background outliers that are functionally irrelevant to the task, thereby improving the fidelity of saliency estimation for each attention projection and mitigating the attention drift induced by quantization.

Finally, we compute column saliency from the rectified Hessian  $\tilde{\mathbf{H}}$  in Eq. (3) and partition each layer into salient and non-salient column sets  $\mathcal{I}_{\text{sal}}$  and  $\mathcal{I}_{\text{non-sal}}$ . The selection proceeds in two stages. First, we form an element-wise importance score that is normalized by the Hessian diagonal and

Table 1: Performance of HBVLA on the CogACT with weight 1.08 bit coversus the other baselines in the SIMPLER environment in terms of success rates (%). “O/C Drawer” refers to the Open/Close Drawer task.  $\Delta$  denotes the relative change with respect to the FP model.

SIMPLER	Method	Pick Coke	Move Near	O/C Drawer	Place Apple	Avg	$\Delta$
Visual Matching	CogACT (FP Model)	91.3	85.0	71.8	50.9	74.8	-
	BiLLM	37.0	45.8	32.4	0.0	28.8	-46
	BiVLM	76.8	62.1	52.7	16.7	57.1	-17.7
	HBLLM	80.7	81.7	64.4	22.2	62.3	-12.5
	HBVLA (ours)	86.7	81.7	71.8	38.4	70.0	-4.8
Variant Aggregation	CogACT (FP Model)	89.6	80.8	28.3	46.6	61.3	-
	BiLLM	21.1	22.2	15.3	0.8	14.9	-46.4
	BiVLM	71.8	67.3	23.1	27.5	47.4	-13.9
	HBLLM	79.3	69.8	24.6	18.0	47.9	-13.4
	HBVLA (ours)	85.1	72.5	21.4	24.9	51.0	-10.3

aggregate it into a per-column score using an  $\ell_2$  reduction, which yields a compact set of candidate salient columns. Second, we determine the final number of salient columns by minimizing a local reconstruction error under our binarization surrogate, and assign the remaining columns to  $\mathcal{I}_{\text{uns}}$ .

### Saliency-Aware Hybrid Binarization With Harr Transform

We use a hybrid binarization method that treats salient and non-salient weights differently, but both parts share the same two-step quantization primitive. We first map weights to the Haar domain and split them into low-pass and high-pass subbands. Concretely, for an even length  $m$ , we define a one-level Haar transform matrix  $\mathbf{H}_m \in \mathbb{R}^{m \times m}$  and map  $w \in \mathbb{R}^{1 \times m}$  to the Haar domain by

$$\mathcal{H}(w) \triangleq w\mathbf{H}_m = [w^{\text{lo}}, w^{\text{hi}}], \quad (10)$$

where  $w^{\text{lo}}, w^{\text{hi}} \in \mathbb{R}^{1 \times (m/2)}$  are the low-pass and high-pass subbands. (more details are provided in Appendix )

After the transform, we employ a row-wise grouping strategy. Instead of global partitioning, we adaptively split coefficients within each frequency band into groups (e.g., dense/sparse) to capture the local structural pattern. Then we apply binarization to every group:

$$Q(u) = \alpha_g \cdot \text{sign}(u - \mu_g), \quad (11)$$

where  $\mu_g$  and  $\alpha_g$  are computed per group. Notably, for non-salient weights, we optimize storage efficiency by enforcing a single shared mean  $\mu$  across groups within the same row and frequency band. This approach effectively reduces the average bit-width and metadata overhead while preserving model performance.

**Non-salient Weights Binarization.** Since salient columns are excluded from the Haar transform of the non-salient part, we first fill the missing values in salient columns using adjacent averages, obtaining  $\mathbf{W}_{l,\text{filled}}$ .

We binarize  $\mathbf{W}_{l,\text{filled}}$  in the Haar domain by applying a row-wise Haar transform along the column axis:

$$\mathbf{W}_{l,\text{non-sal}}^c = \mathcal{H}_{\text{row}}(\mathbf{W}_{l,\text{filled}}) = \mathbf{W}_{l,\text{filled}} \mathbf{H}_m. \quad (12)$$

In VLAs, non-salient columns often exhibit strong modality-dependent structures. However, these columns are typically interleaved in the weight matrix space rather than forming contiguous, modality-specific blocks. This lack of structural locality poses a significant challenge for the Haar transform, which operates on fixed local windows by calculating differences between adjacent columns. When the Haar operator pairs columns from disparate modalities, the resulting cross-modality offsets manifest as sharp step-change outliers in the Harr domain.

To resolve this, we employ a **sparse orthogonal transform**, implemented via a permutation matrix  $\mathbf{P} \in \{0, 1\}^{m \times m}$ , prior to the Haar transform. This mechanism allows us to maintain the  $\mathcal{O}(d)$  convolutional efficiency of Haar while making it adaptive to the underlying weight geometry. After permutation, we follow the quantization primitive:

$$\begin{aligned} \mathbf{U} &= \mathbf{W}_{l,\text{non-sal}} \mathbf{P} \mathbf{H}, \\ \mathbf{U}_B &= Q(\mathbf{U}) = \boldsymbol{\alpha} \odot \text{sign}(\mathbf{U} - \boldsymbol{\mu}), \\ \widehat{\mathbf{W}}_{l,\text{non-sal}} &= \mathbf{U}_B \mathbf{H}^\top \mathbf{P}^\top, \end{aligned} \quad (13)$$

where  $\boldsymbol{\mu}$  and  $\boldsymbol{\alpha}$  are computed group-wise in Eq. (11). Since both the sparse transform  $\mathbf{P}$  and the Haar basis  $\mathbf{H}$  are orthogonal, the Frobenius geometry is strictly preserved, i.e.,  $\|\mathbf{W} - \widehat{\mathbf{W}}\|_F = \|\mathbf{U} - Q(\mathbf{U})\|_F$ .

We construct this sparse orthogonal transform by minimizing the high-frequency energy generated during decomposition. Specifically, for a one-level Haar transform, the energy in the high-pass subband is proportional to the sum of discrepancies between paired columns. Let  $\pi$  be the ordering induced by  $\mathbf{P}$  and let  $\mathbf{H}_{\text{hi}}$  denote the first-level high-pass basis. Then the high-pass energy admits the following iden-

Algorithm 1: Greedy Pairing-and-Chaining for Haar Reordering

---

**Require:**  $W \in \mathbb{R}^{d \times m}$ ; optional  $K$   
**Ensure:** ordering  $\pi \in [m]$

- 1:  $d(i, j) \leftarrow \|W(:, i) - W(:, j)\|_2^2$
- 2: **if**  $K$  is used **then**
- 3:    $\mathcal{N}_K(i) \leftarrow$  top- $K$  neighbors of  $i$  under  $d$
- 4: **end if**
- 5: **Pairing.**  $\mathcal{U} \leftarrow [m]$ ,  $\mathcal{P} \leftarrow \emptyset$
- 6: **while**  $|\mathcal{U}| > 1$  **do**
- 7:   choose  $i \in \mathcal{U}$  (e.g., by descending  $\|W(:, i)\|_2$ )
- 8:    $\mathcal{C} \leftarrow (\mathcal{N}_K(i) \text{ if used else } [m]) \cap (\mathcal{U} \setminus \{i\})$
- 9:   **if**  $\mathcal{C} = \emptyset$  **then**
- 10:      $\mathcal{C} \leftarrow \mathcal{U} \setminus \{i\}$
- 11:   **end if**
- 12:    $j \leftarrow \arg \min_{t \in \mathcal{C}} d(i, t)$
- 13:    $\mathcal{P} \leftarrow \mathcal{P} \cup \{(i, j)\}$ ,  $\mathcal{U} \leftarrow \mathcal{U} \setminus \{i, j\}$
- 14: **end while**
- 15: **if**  $|\mathcal{U}| = 1$  **then**
- 16:    $\mathcal{P} \leftarrow \mathcal{P} \cup \{(r, r)\}$  for leftover  $r$
- 17: **end if**
- 18: **Chaining.** pick seed  $(a, b) \in \mathcal{P}$ , set  $\pi = [a, b]$ , tail =  $b$ ,  $\mathcal{R} = \mathcal{P} \setminus \{(a, b)\}$
- 19: **while**  $\mathcal{R} \neq \emptyset$  **do**
- 20:    $(u, v) \leftarrow \arg \min_{(x, y) \in \mathcal{R}} \min\{d(\text{tail}, x), d(\text{tail}, y)\}$
- 21:   **if**  $d(\text{tail}, u) > d(\text{tail}, v)$  **then**
- 22:     swap  $(u, v)$
- 23:   **end if**
- 24:   append  $u, v$  to  $\pi$ , set tail =  $v$ , remove  $(u, v)$  from  $\mathcal{R}$
- 25: **end while**
- 26: **return**  $\pi$

---

ity:

$$\|\mathbf{W}_{l,\text{non-sal}} \mathbf{P} \mathbf{H}_{\text{hi}}\|_F^2 = \frac{1}{4} \sum_{k=1}^{\lfloor m/2 \rfloor} \|\mathbf{W}_{l,\text{non-sal}}(:, \pi(2k-1)) - \mathbf{W}_{l,\text{non-sal}}(:, \pi(2k))\|_2^2, \quad (14)$$

and we provide a proof in Appendix . Therefore, determining the optimal  $\mathbf{P}$  is equivalent to solving a discrete optimization problem that maximizes local column similarity. Since the exact global optimum is intractable, we adopt a greedy pairing-and-chaining heuristic to efficiently generate the permutation  $\pi$  that defines  $\mathbf{P}$  (see Algorithm 1).

**Salient Weights Binarization** . After obtaining the non-salient approximation  $\widehat{\mathbf{W}}_{l,\text{non-sal}}$ , we quantize salient columns on the residual to avoid interference from the non-salient reconstruction. We define the residual

$$\mathbf{R}_l = \mathbf{W}_l - \widehat{\mathbf{W}}_{l,\text{non-sal}}. \quad (15)$$

By defining  $\mathcal{I}_{\text{sal}}$  as the index set of salient columns, we extract the salient residual  $\mathbf{R}_l(:, \mathcal{I}_{\text{sal}})$  and apply a *column-wise* Haar transform (more details are provided in Appendix ):

$$\mathbf{R}_{l,\text{sal}}^c = \mathbf{H}_n \mathbf{R}_l(:, \mathcal{I}_{\text{sal}}), \quad (16)$$

where  $\mathbf{R}_{l,\text{sal}}^c$  denotes the Haar-domain coefficients of the salient residual. We then apply the same quantization primitive in the Haar domain using a column-wise transform, followed by the inverse transform:

$$\widehat{\mathbf{W}}_{l,\text{sal}} = \mathcal{H}_{\text{col}}^{-1} \left( Q(\mathbf{R}_{l,\text{sal}}^c) \right) = \mathbf{H}_n^{-1} Q(\mathbf{R}_{l,\text{sal}}^c). \quad (17)$$

Finally, we reconstruct the quantized layer weights by summing the two components:

$$\widehat{\mathbf{W}}_l = \widehat{\mathbf{W}}_{l,\text{non-sal}} + \widehat{\mathbf{W}}_{l,\text{sal}}. \quad (18)$$

## Experiment

We validate our approach through a series of experiments across simulated benchmarks and physical robot manipulation tasks. All experiments are conducted on NVIDIA A800 GPUs.

### Experimental Setup

We conduct experiments on three settings: the LIBERO (Liu et al. 2023) and SIMPLER (Li et al. 2024b), two widely recognized robotic manipulation benchmarks for evaluation in simulation environments, and a real-world table-mounted Mobile ALOHA robot with four test tasks, to validate the practical applicability of HBVLA. We use the widely used performance evaluation metrics “Success Rate (SR)” to evaluate the results in these challenging settings.

**LIBERO** (Liu et al. 2023) : This benchmark is designed to evaluate knowledge transfer and policy generalization across four distinct task suites: LIBERO-Spatial, LIBERO-Object, LIBERO-Goal, and LIBERO-Long. It serves as a benchmark for lifelong robot learning, utilizing a Franka Emika Panda arm within the MuJoCo simulator. It contains 5,000 episodes across 100 tasks. To ensure environmental diversity, it leverages procedural generation and provides multimodal data including RGB images, proprioceptive states, and delta actions.

**SIMPLER** (Li et al. 2024b) : This benchmark is designed to bridge the visual and control gaps between reality and simulation by high-fidelity replication of real-world environments, specifically for platforms like the Google robot. The platform offers two evaluation settings: Visual Matching, which minimizes environmental discrepancies to mirror real-world tasks, and Variant Aggregations, which introduces randomized elements, such as lighting, backgrounds, and distractors, to test robustness. We evaluate both settings on a Google robot arm across four manipulation tasks: 1) Pick coke can; 2) Move near; 3) Open/close drawer; and 4) Open top drawer and place apple.

**Real-world Evaluation Suite.** Real-world adaptability is assessed using a stationary Magic dual-arm cobot across three challenging benchmarks (Bu et al. 2025; Zhao et al. 2025): Pick and Place (irregular objects), Sequenced Instruction (e.g., Tower of Hanoi), and Flexible Folding (three-stage towel folding). These tasks test the model’s ability to generalize from a limited dataset (30–450 demonstrations per task) to novel environments.

**Baselines.** We selected recently published 1-bit PTQ methods as baselines, including HBLLM (Chen, Ye, and

Table 2: Performance of HBVLA on the OpenVLA and OpenVLA-OFT with weight 1.08 bit compared with other baselines in the LIBERO benchmark in terms of success rates (%).  $\Delta$  denotes the relative change with respect to the FP model.

Method	Spatial	Object	Goal	Long	Avg	$\Delta$
OpenVLA (FP Model)	84.7	88.4	79.2	53.7	76.5	-
BiLLM	49.1	50.8	52.3	23.2	43.9	-32.6
BiVLM	53.6	55.4	55.9	26.7	47.9	-28.6
HBLLM	65.9	68.4	64.2	35.7	58.6	-17.9
HBVLA (ours)	78.2	81.5	73.6	46.8	70.0	-6.5
OpenVLA-OFT (FP Model)	97.6	98.4	97.9	94.5	97.1	-
BiLLM	59.2	61.4	65.8	44.3	57.7	-39.4
BiVLM	67.8	69.7	68.4	48.9	64.0	-33.1
HBLLM	87.2	76.0	89.6	62.0	79.2	-17.9
HBVLA (ours)	89.3	97.8	91.3	82.7	90.3	-6.8

Jiang 2025), BiLLM (Huang et al. 2024), and BiVLM (Wang et al. 2025b). BiLLM and HBLLM all utilize the PTQ approach for model calibration through OBQ based method of GPTQ. For calibration, we randomly sample 256 trajectories from the benchmark’s training set to form the calibration set. During quantization, we set the block size to 128 in BiLLM and HBLLM. For HBLLM, we adopt the row-wise shared-mean configuration with column  $\ell_2$ -norm saliency (40 candidates). For BiVLM, we adapt salient weights to 5% for the language encoder and 1% for vision, aligning with VLA-specific sensitivity profiles. Given this varying sensitivity, all comparisons with SOTA quantization methods are conducted by quantizing only the vision backbone and language backbone, leaving other components in full precision. We adopt the convolution-based Haar transform from HBLLM, utilizing fixed kernels ( $h_{lo} = [0.5, 0.5]$ ,  $h_{hi} = [0.5, -0.5]$ ) with stride 2.

**Implementation Details.** Our floating-point (FP) baseline employs models with weights in the BF16 format. For two simulation benchmarks, we employ the official checkpoints of OpenVLA, OpenVLA-OFT, and CogACT as the base model to do the quantization. For the real-world evaluation suite, following (Kim, Finn, and Liang 2025), we use the official OpenVLA checkpoints as initialization to train the OpenVLA-OFT baseline. Specifically, we apply the LoRA technique with a rank of 32 to the vision encoder and LLM backbone, while the action head and proprioceptive projector are fully optimized. The action chunk size is set to 20. The model is trained for 100,000 gradient steps with a batch size 64, and an initial learning rate of 5e-4, which decayed to 5e-5 after 50,000 steps. Then the quantization methods are based on this baseline model. We introduce the detailed instructions and descriptions for the three task suites in our Mobile ALOHA experiments. For the Pick and Place task (450 demonstrations), the robot will place the bucket in the center and put the simulated toy objects of which the instruction has given (yellow banana, green pepper, purple eggplant) into the bucket. The corresponding instructions is

“put X into bucket”. For the Sequenced Instruction task (60 demonstrations), the robot will stack the medium tower on top of the large one first, and then stack the small one on top of the medium one. The corresponding instructions is “stack tower of hanoi”. For the Sequenced Instruction task (30 demonstrations), the robot will first fold the towel vertically, then fold horizontally, and finally flatten it. The corresponding instructions is “fold towel twice”.

## Main Results

**LIBERO.** We present quantization results in Table 2. Our HBVLA consistently outperforms prior low-bit baselines on both OpenVLA (Kim et al. 2024) and OpenVLA-OFT (Kim, Finn, and Liang 2025) across all four task suites (Spatial/Object/Goal/Long), yielding 11.1%–32.6% higher average success rates. More importantly, HBVLA substantially narrows the gap to full-precision performance, incurring only a small degradation while remaining markedly closer to the FP model than existing quantization methods. We also observe strong robustness on the challenging long-horizon suite, suggesting that HBVLA better preserves action-critical representations and policy fidelity under aggressive compression, leading to improved transfer and generalization across diverse manipulation tasks.

**SIMPLER.** Table 1 reports results on SIMPLER with CogACT (Li et al. 2024a) under quantization. Overall, HBVLA achieves the best average performance among all across both Visual Matching and Variant Aggregation, with 3.1%–41.2% absolute improvements in average success rate. In Visual Matching, HBVLA reaches 70.0% average success, surpassing HBLLM (62.3%), BiVLM (57.1%), and BiLLM (28.8%), while remaining close to the full-precision model. In the more challenging *Variant Aggregation* setting, although HBVLA is slightly lower than HBLLM and BiVLM on certain individual tasks (e.g., O/C Drawer), it delivers the highest overall average success rate. These results indicate that HBVLA strikes a favorable balance between compression and accuracy: it largely preserves near-full-precision fi-

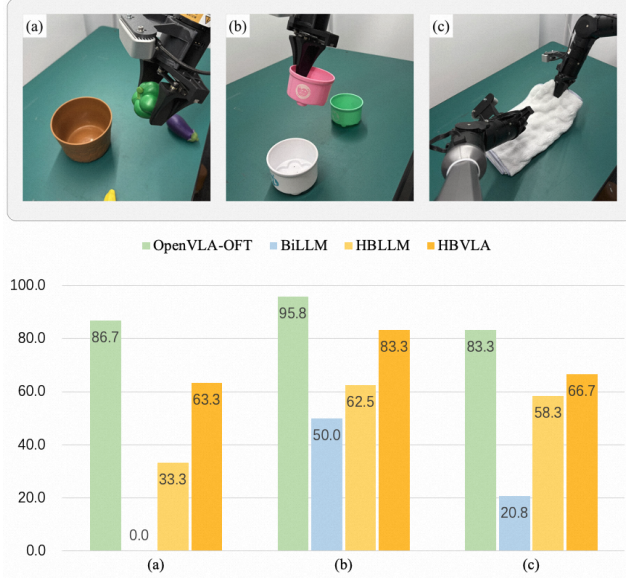


Figure 3: Comparison on the Mobile ALOHA experiments. Evaluation across three real-world tasks, including (a) Pick and Place, (b) Sequenced Instruction, (c) Flexible Folding. **Top:** Middle state image for each task. **Bottom:** Task-specific success rates for OpenVLA-OFT (FP Model), our HBVLA method, and baselines, including BiLLM and HBLLM.

delity while still improving overall robustness and generalization compared to existing low-bit methods.

**Mobile ALOHA.** The Pick and Place task is evaluated for a total of 30 trials (10 per object), while other tasks are evaluated for 24 trials each. The experimental results on real-world tasks are reported in Figure 3. The results show that OpenVLA-OFT achieves high success rates on three tasks. Consistent with the simulation results, BiLLM exhibits the poorest performance across the three tasks. We observed that the robotic arm suffered from persistent oscillations during execution, which directly led to its failure in the Pick and Place task. While our proposed HBVLA method exhibits only a marginal decrease in success rate across these tasks relative to the FP model, it substantially outperforms other baselines, thereby validating the effectiveness of our approach.

## Further Analysis

**Sensitivity Analysis.** As shown in Figure 4, the vision encoder proves to be the most robust to quantization, maintaining performance stability. In contrast, the language model exhibits considerable sensitivity. Most critically, the projector and action head demonstrate the highest sensitivity, where even minor precision loss leads to severe degradation.

**Column-Norm Criterion for Permutation.** To evaluate the impact of the permutation criterion for non-salient columns on quantization effectiveness, we compare two strategies: the column  $\ell_1$ -norm and the column  $\ell_2$ -norm. The results are shown in Table 3. Using the  $\ell_2$ -norm yields lower quantization error and superior downstream perfor-

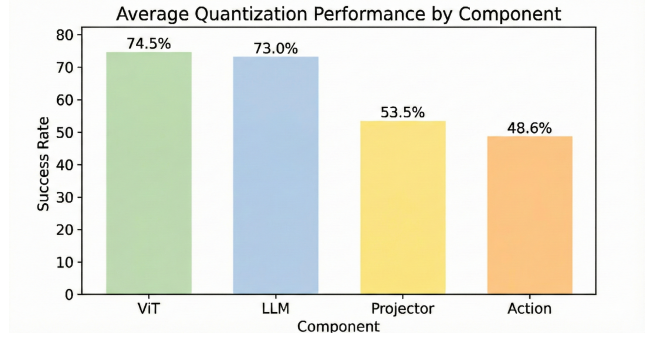


Figure 4: Compared with the FP (full-precision) baseline achieving a 74.8% task success rate, quantizing different components of CogACT in SimpleRenv leads to varying degrees of performance degradation.

mance compared to  $\ell_1$ , as the  $\ell_2$ -norm more effectively captures energy distribution across columns, thereby improving quantization quality.

Table 3: Study of non-salient column permutation criterion

Selection criterion	Visual Matching $\downarrow$	Variant Aggregation $\downarrow$
$\ell_1$	11.6%	15.6%
$\ell_2$	<b>8.8%</b>	<b>12.8%</b>

**Effectiveness of Policy-Aware Hessian.** To investigate the impact of the proposed rectified Hessian on saliency estimation, we compare it against the standard Hessian formulation. As shown in Table 4, our policy-aware Hessian effectively filters out quantization noise and accurately identifies task-critical weights essential for instruction-following control, resulting in significant gains in success rate.

Table 4: Study of Hessian formulation on quantization

Hessian Formulation	Visual Matching $\downarrow$	Variant Aggregation $\downarrow$
Standard	12.5%	13.4%
Policy-Aware	<b>10.3%</b>	<b>12.1%</b>

## Conclusion

In this paper, we presented HBVLA, a novel 1-bit post-training quantization framework tailored for VLA models. We address action degradation in extreme quantization via a policy-aware weight partitioning strategy, utilizing a rectified Hessian to protect weights critical to action generation. Furthermore, we propose a sparse orthogonal transform to optimize weight geometry in the Haar domain, suppressing high-pass noise and modality heterogeneity. Extensive experiments across LIBERO, SIMPLER, and real-world Mobile ALOHA platforms demonstrate that HBVLA consistently achieves SOTA. This work provides a practical foundation for deploying large-scale VLA models on resource-constrained robotic platforms.

## References

Bengio, Y.; Leonard, N.; and Courville, A. 2013. Estimating or propagating gradients through stochastic neurons for conditional computation. *ArXiv preprint arXiv:1308.3432*.

Black, K.; Brown, N.; Driess, D.; Esmail, A.; Equi, M.; Finn, C.; Fusai, N.; Groom, L.; Hausman, K.; Ichter, B.; Jakubczak, S.; Jones, T.; Ke, L.; Levine, S.; Li-Bell, A.; Mothukuri, M.; Nair, S.; Pertsch, K.; Shi, L. X.; Tanner, J.; Vuong, Q.; Walling, A.; Wang, H.; and Zhilinsky, U. 2026.  $\pi_0$ : A Vision-Language-Action Flow Model for General Robot Control. *arXiv:2410.24164*.

Bu, Q.; Yang, Y.; Cai, J.; Gao, S.; Ren, G.; Yao, M.; Luo, P.; and Li, H. 2025. Univla: Learning to act anywhere with task-centric latent actions. *arXiv preprint arXiv:2505.06111*.

Chen, N.; Ye, W.; and Jiang, Y. 2025. HBLLM: Wavelet-Enhanced High-Fidelity 1-Bit Quantization for LLMs. In Courville, A.; and Lawrence, N. D., eds., *Proceedings of the Thirty-ninth Annual Conference on Neural Information Processing Systems (NeurIPS 2025)*. Vancouver, Canada: Curran Associates.

Courbariaux, M.; Bengio, Y.; and David, J.-P. 2015. Binaryconnect: Training deep neural networks with binary weights during propagations. In Cortes, C.; and Lawrence, N., eds., *Proceedings of Advances in Neural Information Processing Systems (NeurIPS 2015)*, volume 28. Montreal, Canada: Curran Associates.

Fang, H.; Liu, Y.; Du, Y.; Du, L.; and Yang, H. 2025. Sqap-vla: A synergistic quantization-aware pruning framework for high-performance vision-language-action models. *arXiv preprint arXiv:2509.09090*.

Huang, W.; Liu, Y.; Qin, H.; Li, Y.; Zhang, S.; Liu, X.; Magno, M.; and Qi, X. 2024. BiLLM: Pushing the Limit of Post-Training Quantization for LLMs. In Krause, A.; and Brunskill, E., eds., *Proceedings of the International Conference on Machine Learning (ICML 2024)*. Vienna, Austria: OpenReview.net.

Jacob, B.; Kligys, S.; Chen, B.; Zhu, M.; Tang, M.; Howard, A.; Adam, H.; and Kalenichenko, D. 2018. Quantization and training of neural networks for efficient integer-arithmetic-only inference. In *Proceedings of the IEEE conference on computer vision and pattern recognition*, 2704–2713.

Karamcheti, S.; Nair, S.; Balakrishna, A.; Liang, P.; Kollar, T.; and Sadigh, D. 2024. Prismatic vlms: Investigating the design space of visually-conditioned language models. In *Forty-first International Conference on Machine Learning*.

Kim, M. J.; Finn, C.; and Liang, P. 2025. Fine-tuning vision-language-action models: Optimizing speed and success. *arXiv preprint arXiv:2502.19645*.

Kim, M. J.; Pertsch, K.; Karamcheti, S.; Xiao, T.; Balakrishna, A.; Nair, S.; Rafailov, R.; Foster, E.; Lam, G.; Sanketi, P.; et al. 2024. Openvla: An open-source vision-language-action model. *arXiv preprint arXiv:2406.09246*.

Krishnamoorthi, R. 2018. Quantizing deep convolutional networks for efficient inference: A whitepaper. *arXiv preprint arXiv:1806.08342*.

Li, Q.; Liang, Y.; Wang, Z.; Luo, L.; Chen, X.; Liao, M.; Wei, F.; Deng, Y.; Xu, S.; Zhang, Y.; et al. 2024a. Cogact: A foundational vision-language-action model for synergizing cognition and action in robotic manipulation. *arXiv preprint arXiv:2411.19650*.

Li, X.; Hsu, K.; Gu, J.; Pertsch, K.; Mees, O.; Walke, H. R.; Fu, C.; Lunawat, I.; Sieh, I.; Kirmani, S.; et al. 2024b. Evaluating real-world robot manipulation policies in simulation. *arXiv preprint arXiv:2405.05941*.

Li, Z.; Yan, X.; Zhang, T.; Qin, H.; Xie, D.; Tian, J.; Shi, Z.; Kong, L.; Zhang, Y.; and Yang, X. 2025. ARB-LLM: Alternating Refined Binarizations for Large Language Models. In Cho, K.; and Lamb, A., eds., *Proceedings of the Thirteenth International Conference on Learning Representations (ICLR 2025)*. Singapore: OpenReview.net.

Lin, J.; Tang, J.; Tang, H.; Yang, S.; Chen, W.-M.; Wang, W.-C.; Xiao, G.; Dang, X.; Gan, C.; and Han, S. 2024. Awq: Activation-aware weight quantization for on-device llm compression and acceleration. *Proceedings of machine learning and systems*, 6: 87–100.

Liu, B.; Zhu, Y.; Gao, C.; Feng, Y.; Liu, Q.; Zhu, Y.; and Stone, P. 2023. Libero: Benchmarking knowledge transfer for lifelong robot learning. *Advances in Neural Information Processing Systems*, 36: 44776–44791.

Liu, J.; Pan, Z.; He, H.; Cai, J.; and Zhuang, B. 2022a. Ecoformer: Energy-saving attention with linear complexity. In Koyejo, S.; and Mohamed, S., eds., *Proceedings of Advances in Neural Information Processing Systems (NeurIPS 2022)*, volume 35, 10295–10308. New Orleans, LA, USA: Curran Associates.

Liu, Z.; Oguz, B.; Pappu, A.; Xiao, L.; Yih, S.; Li, M.; Krishnamoorthi, R.; and Mehdad, Y. 2022b. Bit: Robustly binarized multi-distilled transformer. In Koyejo, S.; and Mohamed, S., eds., *Proceedings of Advances in Neural Information Processing Systems (NeurIPS 2022)*, volume 35, 14303–14316. New Orleans, LA, USA: Curran Associates.

Nagel, M.; Amjad, R. A.; Van Baalen, M.; Louizos, C.; and Blankevoort, T. 2020. Up or down? adaptive rounding for post-training quantization. In *International conference on machine learning*, 7197–7206. PMLR.

Nagel, M.; Baalen, M. v.; Blankevoort, T.; and Welling, M. 2019. Data-free quantization through weight equalization and bias correction. In *Proceedings of the IEEE/CVF international conference on computer vision*, 1325–1334.

Park, S.; Kim, H.; Kim, S.; Jeon, W.; Yang, J.; Jeon, B.; Oh, Y.; and Choi, J. 2025. Saliency-aware quantized imitation learning for efficient robotic control. In *Proceedings of the IEEE/CVF International Conference on Computer Vision*, 13140–13150.

Rastegari, M.; Ordonez, V.; Redmon, J.; and Farhadi, A. 2016. XNOR-Net: ImageNet Classification Using Binary Convolutional Neural Networks. In Leibe, B.; Matas, J.; Sebe, N.; and Welling, M., eds., *Proceedings of the 14th European Conference on Computer Vision (ECCV 2016)*, volume 9908, 525–542. Amsterdam, The Netherlands: Springer.

Team, O. M.; Ghosh, D.; Walke, H.; Pertsch, K.; Black, K.; Mees, O.; Dasari, S.; Hejna, J.; Kreiman, T.; Xu, C.; et al. 2024. Octo: An open-source generalist robot policy. *arXiv preprint arXiv:2405.12213*.

Vaswani, A.; Shazeer, N.; Parmar, N.; Uszkoreit, J.; Jones, L.; Gomez, A. N.; Kaiser, L.; and Polosukhin, I. 2017. Attention is all you need. In Guyon, I.; and Luxburg, U. V., eds., *Proceedings of Advances in Neural Information Processing Systems (NeurIPS 2017)*, volume 30. Long Beach, CA, USA: Curran Associates.

Wang, H.; Xiong, C.; Wang, R.; and Chen, X. 2025a. BitVLA: 1-bit Vision-Language-Action Models for Robotics Manipulation. *arXiv preprint arXiv:2506.07530*.

Wang, X.; Huang, J.; Abdalla, R.; Zhang, C.; Xian, R.; and Manocha, D. 2025b. Bi-VLM: Pushing Ultra-Low Precision Post-Training Quantization Boundaries in Vision-Language Models. *arXiv preprint arXiv:2509.18763*.

Xue, Y.; Huang, Y.; Shao, J.; and Zhang, J. 2025. VLMQ: Efficient Post-Training Quantization for Large Vision-Language Models via Hessian Augmentation. *arXiv preprint arXiv:2508.03351*.

Yuan, Z.; Shang, Y.; and Dong, Z. 2024. PB-LLM: Partially Binarized Large Language Models. In Gupta, A.; and Guyon, I. M., eds., *Proceedings of the Twelfth International Conference on Learning Representations (ICLR 2024)*. Vienna, Austria: OpenReview.net.

Zhao, Q.; Lu, Y.; Kim, M. J.; Fu, Z.; Zhang, Z.; Wu, Y.; Li, Z.; Ma, Q.; Han, S.; Finn, C.; et al. 2025. Cot-vla: Visual chain-of-thought reasoning for vision-language-action models. In *Proceedings of the Computer Vision and Pattern Recognition Conference*, 1702–1713.

Zitkovich, B.; Yu, T.; Xu, S.; Xu, P.; Xiao, T.; Xia, F.; Wu, J.; Wohlhart, P.; Welker, S.; Wahid, A.; et al. 2023. Rt-2: Vision-language-action models transfer web knowledge to robotic control. In *Conference on Robot Learning*, 2165–2183. PMLR.

## Derivations for Hessian Rectification

### Proof of the Importance-Aware Weight Update (Eq. (28))

Let  $\mathbf{G} \in \mathbb{R}^{N \times N}$  be a diagonal importance matrix, and define

$$\tilde{\mathbf{X}} = \mathbf{X}\mathbf{G}^{1/2}, \quad \tilde{\mathbf{r}} = \mathbf{r}\mathbf{G}^{1/2}, \quad \mathbf{H}_e = \mathbf{X}\mathbf{G}\mathbf{X}^\top = \tilde{\mathbf{X}}\tilde{\mathbf{X}}^\top. \quad (19)$$

Consider the constrained objective (same as the main text) with the constraint on the  $q$ -th element:

$$\min_{\Delta\mathbf{w}} \left\| (\Delta\mathbf{w}\mathbf{X} - \mathbf{r})\mathbf{G}^{1/2} \right\|_2^2 \quad \text{s.t.} \quad \Delta\mathbf{w}\mathbf{e}_q^\top + w_q - \hat{w}_q = 0, \quad (20)$$

where  $\mathbf{e}_q$  is the one-hot vector.

**Lagrangian.** The Lagrangian is

$$\mathcal{L} = \left\| (\Delta\mathbf{w}\mathbf{X} - \mathbf{r})\mathbf{G}^{1/2} \right\|_2^2 + \lambda (\Delta\mathbf{w}\mathbf{e}_q^\top + w_q - \hat{w}_q). \quad (21)$$

**KKT conditions.** Differentiate w.r.t.  $\Delta\mathbf{w}$  and  $\lambda$ , and set to zero:

$$\frac{\partial \mathcal{L}}{\partial \Delta\mathbf{w}} = 2\Delta\mathbf{w}\mathbf{H}_e - 2\tilde{\mathbf{r}}\tilde{\mathbf{X}}^\top + \lambda\mathbf{e}_q = 0, \quad (22)$$

$$\frac{\partial \mathcal{L}}{\partial \lambda} = \Delta\mathbf{w}\mathbf{e}_q^\top + w_q - \hat{w}_q = 0. \quad (23)$$

From (22) we have

$$\Delta\mathbf{w}\mathbf{H}_e = \tilde{\mathbf{r}}\tilde{\mathbf{X}}^\top - \frac{\lambda}{2}\mathbf{e}_q. \quad (24)$$

Multiplying (24) by  $\mathbf{H}_e^{-1}$  on the right gives

$$\Delta\mathbf{w} = \tilde{\mathbf{r}}\tilde{\mathbf{X}}^\top\mathbf{H}_e^{-1} - \frac{\lambda}{2}\mathbf{e}_q\mathbf{H}_e^{-1}. \quad (25)$$

**Solve for  $\lambda$  using the constraint.** Right-multiply (25) by  $\mathbf{e}_q^\top$  and use (23):

$$\tilde{\mathbf{r}}\tilde{\mathbf{X}}^\top\mathbf{H}_e^{-1}\mathbf{e}_q^\top - \frac{\lambda}{2}\mathbf{e}_q\mathbf{H}_e^{-1}\mathbf{e}_q^\top = \hat{w}_q - w_q. \quad (26)$$

Noting that  $\mathbf{e}_q\mathbf{H}_e^{-1}\mathbf{e}_q^\top = (\mathbf{H}_e^{-1})_{qq}$ , we obtain

$$\frac{\lambda}{2} = \frac{\tilde{\mathbf{r}}\tilde{\mathbf{X}}^\top\mathbf{H}_e^{-1}\mathbf{e}_q^\top - (\hat{w}_q - w_q)}{(\mathbf{H}_e^{-1})_{qq}}. \quad (27)$$

**Plug back to get the closed-form update.** Substitute (27) into (25) and rearrange terms, yielding the standard Hessian-guided closed-form update with the importance-aware Hessian  $\mathbf{H}_e$ :

$$\Delta\mathbf{w} = (\hat{w}_q - w_q) \frac{(\mathbf{H}_e^{-1})_{q:}}{(\mathbf{H}_e^{-1})_{qq}} + \tilde{\mathbf{r}}\tilde{\mathbf{X}}^\top(\mathbf{H}_e^{-1})_{-q}. \quad (28)$$

This completes the proof.

### Proof of Theorem 1

**Theorem 1** (Connection between block-wise loss perturbation and output error). *Let  $\mathcal{L}_{\text{Block}}(\boldsymbol{\theta})$  be the block-wise loss and let  $\Delta\boldsymbol{\theta}$  be the quantization-induced perturbation. Then the loss perturbation admits a first-order approximation*

$$\Delta\mathcal{L}_{\text{Block}} \approx \Delta\boldsymbol{\theta} \mathbf{p}_{(\Delta\boldsymbol{\theta})}^\top \approx \Delta\mathbf{z} \mathbf{p}_{(\Delta\mathbf{z})}^\top, \quad (29)$$

where  $\mathbf{z}$  denotes the block output and  $\Delta\mathbf{z}$  the induced output error.

*Proof.* Using the Taylor expansion of  $\mathcal{L}_{\text{Block}}$  at  $\boldsymbol{\theta}$ ,

$$\Delta\mathcal{L}_{\text{Block}} = \mathcal{L}_{\text{Block}}(\boldsymbol{\theta} + \Delta\boldsymbol{\theta}) - \mathcal{L}_{\text{Block}}(\boldsymbol{\theta}) \quad (30)$$

$$= \Delta\boldsymbol{\theta} \mathbf{p}_{(\Delta\boldsymbol{\theta})}^\top + \mathcal{O}(\|\Delta\boldsymbol{\theta}\|^2). \quad (31)$$

Ignoring higher-order terms gives the first-order approximation. Next, by the chain rule, writing the block output as  $\mathbf{z} = \mathbf{z}(\boldsymbol{\theta})$ ,

$$\Delta\mathcal{L}_{\text{Block}} \approx \sum_{i=1}^D \Delta\theta_i \frac{\partial \mathcal{L}_{\text{Block}}}{\partial \theta_i} = \sum_{i=1}^D \Delta\theta_i \left( \sum_{j=1}^Q \frac{\partial \mathcal{L}_{\text{Block}}}{\partial z_j} \frac{\partial z_j}{\partial \theta_i} \right) \quad (32)$$

$$= \sum_{j=1}^Q \frac{\partial \mathcal{L}_{\text{Block}}}{\partial z_j} \left( \sum_{i=1}^D \Delta\theta_i \frac{\partial z_j}{\partial \theta_i} \right) = \sum_{j=1}^Q \frac{\partial \mathcal{L}_{\text{Block}}}{\partial z_j} \Delta z_j = \Delta\mathbf{z} \mathbf{p}_{(\Delta\mathbf{z})}^\top. \quad (33)$$

The proof is complete.  $\square$

## Details of the One-Level Haar Transform via Strided Convolutions

### Notation

Let  $m$  be an even integer and let  $w \in \mathbb{R}^{1 \times m}$  denote a row vector. We use 0-based indexing for clarity:

$$w = [w_0, w_1, \dots, w_{m-1}].$$

Define  $J \triangleq m/2$ . The one-level Haar transform maps  $w$  into two subbands: a low-pass part  $w^{\text{lo}} \in \mathbb{R}^{1 \times J}$  and a high-pass part  $w^{\text{hi}} \in \mathbb{R}^{1 \times J}$ .

### Matrix Form of the One-Level Haar Transform

We define a one-level Haar transform matrix  $\mathbf{H}_m \in \mathbb{R}^{m \times m}$  as

$$\mathbf{H}_m \triangleq [\mathbf{L}_m \ \mathbf{G}_m], \quad \mathbf{L}_m, \mathbf{G}_m \in \mathbb{R}^{m \times J}, \quad (34)$$

where  $\mathbf{L}_m$  (analysis low-pass) and  $\mathbf{G}_m$  (analysis high-pass) are sparse matrices that operate on adjacent pairs. Concretely, for each  $k = 0, 1, \dots, J-1$ ,

$$(\mathbf{L}_m)_{2k, k} = \frac{1}{2}, \quad (\mathbf{L}_m)_{2k+1, k} = \frac{1}{2}, \quad (35)$$

$$(\mathbf{G}_m)_{2k, k} = \frac{1}{2}, \quad (\mathbf{G}_m)_{2k+1, k} = -\frac{1}{2}, \quad (36)$$

and all other entries are zero.

With this construction, the Haar-domain representation is

$$\mathcal{H}(w) \triangleq w\mathbf{H}_m = [w^{\text{lo}}, w^{\text{hi}}], \quad (37)$$

where

$$w^{\text{lo}} = w\mathbf{L}_m, \quad w^{\text{hi}} = w\mathbf{G}_m. \quad (38)$$

### Closed-Form Pairwise Computation

From the sparsity pattern above, each coefficient depends only on a length-2 window: for  $k = 0, 1, \dots, J-1$ ,

$$w_k^{\text{lo}} = \frac{1}{2}(w_{2k} + w_{2k+1}), \quad (39)$$

$$w_k^{\text{hi}} = \frac{1}{2}(w_{2k} - w_{2k+1}). \quad (40)$$

Hence, the transform is a pairwise “average and difference” decomposition.

### Implementation as Two Fixed 1D Convolutions (Stride 2)

Equations (39)–(40) are exactly equivalent to two *fixed* 1D convolutions with kernel size 2 and stride 2:

$$h^{\text{lo}} = \left[ \frac{1}{2}, \frac{1}{2} \right], \quad h^{\text{hi}} = \left[ \frac{1}{2}, -\frac{1}{2} \right]. \quad (41)$$

Using “valid” convolution (no padding) with stride 2, the outputs are

$$w_k^{\text{lo}} = \sum_{t=0}^1 h_t^{\text{lo}} w_{2k+t} = \frac{1}{2}w_{2k} + \frac{1}{2}w_{2k+1}, \quad (42)$$

$$w_k^{\text{hi}} = \sum_{t=0}^1 h_t^{\text{hi}} w_{2k+t} = \frac{1}{2}w_{2k} - \frac{1}{2}w_{2k+1}, \quad (43)$$

for  $k = 0, 1, \dots, J-1$ . Therefore,  $\mathcal{H}(w)$  can be computed by applying these two kernels along the last dimension of  $w$  with stride 2, producing the low-pass and high-pass subbands, respectively.

### Inverse Transform (Synthesis)

Given  $(w^{\text{lo}}, w^{\text{hi}})$ , the original samples can be reconstructed pairwise. Solving (39)–(40) yields, for each  $k = 0, 1, \dots, J-1$ ,

$$w_{2k} = w_k^{\text{lo}} + w_k^{\text{hi}}, \quad (44)$$

$$w_{2k+1} = w_k^{\text{lo}} - w_k^{\text{hi}}. \quad (45)$$

Equivalently, if we concatenate  $c \triangleq [w^{\text{lo}}, w^{\text{hi}}] \in \mathbb{R}^{1 \times m}$ , then  $w = c\mathbf{H}_m^{-1}$ , where  $\mathbf{H}_m^{-1}$  is the blockwise inverse induced by the  $2 \times 2$  inverse on each adjacent pair.

## Row-Wise Application to a Weight Matrix

For a weight matrix  $\mathbf{W} \in \mathbb{R}^{d \times m}$  (with even  $m$ ), a *row-wise* one-level Haar transform applies (37) independently to each row:

$$\mathcal{H}_{\text{row}}(\mathbf{W}) \triangleq \mathbf{W}\mathbf{H}_m = [\mathbf{W}^{\text{lo}}, \mathbf{W}^{\text{hi}}], \quad (46)$$

where  $\mathbf{W}^{\text{lo}}, \mathbf{W}^{\text{hi}} \in \mathbb{R}^{d \times (m/2)}$ . In practice, this is implemented by running the two fixed stride-2 convolutions in Section along the column dimension for each row.

## Column-Wise Application to a Weight Matrix

For a weight matrix  $\mathbf{W} \in \mathbb{R}^{d \times m}$  (with even  $d$ ), a *column-wise* one-level Haar transform applies the same one-level Haar transform (37) independently to each column:

$$\mathcal{H}_{\text{col}}(\mathbf{W}) \triangleq \mathbf{H}_d^\top \mathbf{W} = \begin{bmatrix} \mathbf{W}^{\text{lo}} \\ \mathbf{W}^{\text{hi}} \end{bmatrix}, \quad (47)$$

where  $\mathbf{W}^{\text{lo}}, \mathbf{W}^{\text{hi}} \in \mathbb{R}^{(d/2) \times m}$  are the low-pass and high-pass subbands along the *row* dimension (i.e., obtained by pairwise averaging/differencing adjacent rows for each fixed column).

Equivalently, column-wise Haar can be implemented by applying the two fixed stride-2 1D convolutions in Section along the *row* dimension (for each column), or by transposition:

$$\mathcal{H}_{\text{col}}(\mathbf{W}) = (\mathcal{H}_{\text{row}}(\mathbf{W}^\top))^\top. \quad (48)$$

In practice, this is implemented by running the two fixed stride-2 convolutions with kernels  $h^{\text{lo}}, h^{\text{hi}}$  along the first dimension of  $\mathbf{W}$  (treating each column as a 1D signal), producing  $\mathbf{W}^{\text{lo}}$  and  $\mathbf{W}^{\text{hi}}$  respectively.

## One-level Haar Identity and the High-pass Energy (Proof)

We give a short proof of the identity used in Eq. (14). Let  $\mathbf{W} \in \mathbb{R}^{d \times m}$  be a weight matrix whose columns are  $w_1, \dots, w_m$ . Let  $P \in \{0, 1\}^{m \times m}$  be a permutation matrix and let  $\pi$  be the induced ordering, so that

$$WP = [w_{\pi(1)}, w_{\pi(2)}, \dots, w_{\pi(m)}].$$

We consider a one-level 1D Haar transform applied along the column axis, which corresponds to right-multiplication by an orthogonal Haar matrix  $H \in \mathbb{R}^{m \times m}$ .

**One-level Haar structure.** Assume  $m$  is even for simplicity. The one-level Haar matrix can be written as

$$H = [H_{\text{lo}}, H_{\text{hi}}],$$

where  $H_{\text{lo}}, H_{\text{hi}} \in \mathbb{R}^{m \times (m/2)}$  are the low-pass and high-pass bases. The high-pass basis  $H_{\text{hi}}$  has the following form

$$H_{\text{hi}} = \frac{1}{2} \begin{bmatrix} 1 & 0 & 0 & \cdots & 0 \\ -1 & 0 & 0 & \cdots & 0 \\ 0 & 1 & 0 & \cdots & 0 \\ 0 & -1 & 0 & \cdots & 0 \\ \vdots & \vdots & \vdots & \ddots & \vdots \\ 0 & 0 & 0 & \cdots & 1 \\ 0 & 0 & 0 & \cdots & -1 \end{bmatrix}.$$

Equivalently, the  $k$ -th column of  $H_{\text{hi}}$  has nonzeros only at rows  $2k-1$  and  $2k$  with values  $+1/2$  and  $-1/2$ .

**High-pass coefficients are pairwise differences.** Define the one-level high-pass coefficients of  $WP$  as

$$U_{\text{hi}} = WP H_{\text{hi}} \in \mathbb{R}^{d \times (m/2)}.$$

Let  $u_{\text{hi}}^{(k)}$  denote the  $k$ -th column of  $U_{\text{hi}}$ . By the explicit structure of  $H_{\text{hi}}$ , we have

$$\begin{aligned} u_{\text{hi}}^{(k)} &= WP h_{\text{hi}}^{(k)} \\ &= \frac{1}{2} (WP(:, 2k-1) - WP(:, 2k)) \\ &= \frac{1}{2} (w_{\pi(2k-1)} - w_{\pi(2k)}). \end{aligned}$$

So each one-level Haar high-pass coefficient is exactly a scaled difference between the two columns in the corresponding local window.

**High-pass energy reduces to a sum of within-pair discrepancies.** Using the definition of the Frobenius norm,

$$\|U_{\text{hi}}\|_F^2 = \sum_{k=1}^{m/2} \|u_{\text{hi}}^{(k)}\|_2^2,$$

and substituting the expression above, we obtain

$$\begin{aligned} \|WPH_{\text{hi}}\|_F^2 &= \sum_{k=1}^{m/2} \left\| \frac{1}{2} (w_{\pi(2k-1)} - w_{\pi(2k)}) \right\|_2^2 \\ &= \frac{1}{4} \sum_{k=1}^{m/2} \|w_{\pi(2k-1)} - w_{\pi(2k)}\|_2^2. \end{aligned}$$

This proves that the one-level high-pass energy is proportional to the sum of squared discrepancies inside each Haar pair, which gives Eq. (14).

**Odd  $m$ .** If  $m$  is odd, one can apply the same derivation to the first  $2\lfloor m/2 \rfloor$  columns and keep one leftover column unchanged or pad one dummy column. This only affects a constant number of terms and does not change the conclusion.

**Why nearest-neighbor pairing and chaining.** The identity above shows that, for one-level Haar, the high-pass energy is controlled by the within-pair distances

$$\sum_k \|w_{\pi(2k-1)} - w_{\pi(2k)}\|_2^2.$$

Therefore, a natural strategy is to first form disjoint pairs of columns that minimize these distances, which matches the nearest-neighbor *pairing* step. After the pairs are formed, we still need a global order  $\pi$ . The *chaining* step then orders the pairs and chooses their orientation to avoid large jumps at pair boundaries, which helps reduce additional discontinuities beyond the first-level windows.